ADVANCED MATERIALS

Supporting Information

for *Adv. Mater.,* DOI: 10.1002/adma.202102139

Ultrastrong and Ductile Soft Magnetic High-Entropy Alloys via Coherent Ordered Nanoprecipitates

Liuliu Han, Ziyuan Rao, Isnaldi R. Souza Filho, Fernando Maccari, Ye Wei, Ge Wu, Ali Ahmadian, Xuyang Zhou, Oliver Gutfleisch, Dirk Ponge, Dierk Raabe, and Zhiming Li**

WILEY-VCH

Supporting Information

Ultrastrong and ductile soft magnetic high-entropy alloys via coherent ordered nanoprecipitates

Liuliu Han[1], Ziyuan Rao[1], Isnaldi R. Souza Filho[1], Fernando Maccari[2], Ye Wei[1], Ge Wu[1], Ali Ahmadian[1], Xuyang Zhou[1], Oliver Gutfleisch[2], Dirk Ponge[1], Dierk Raabe[1*], Zhiming Li[3,4*]

1. Max-Planck-Institut für Eisenforschung, Max-Planck-Straße 1, 40237 Düsseldorf, Germany
2. Functional Materials, Materials Science, Technical University of Darmstadt, 64287 Darmstadt, Germany
3. School of Materials Science and Engineering, Central South University, 410083 Changsha, China
4. Key Laboratory of Nonferrous Metal Materials Science and Engineering, Ministry of Education, Central South University, Changsha, 410083, China

[*]*Correspondence to: d.raabe@mpie.de (D. Raabe); lizhiming@csu.edu.cn (Z. Li)*

Experimental Section

Material preparation: The bulk alloy ingots were synthesized in a vacuum induction furnace using pure metals (purity above 99.8%) under a high-purity argon atmosphere. The alloys were analyzed by the wet-chemical method with chemical compositions shown in **Table S**1. The alloy ingots with the dimensions of 40 × 25 × 10 mm^3 were then hot-rolled at 1473 K to a thickness reduction from 10 mm to 5 mm. The alloy sheets were then homogenized at 1473 K for 10 min under the argon's protection, followed by water-quenching.

Mechanical characterization: Uniaxial tensile tests were performed at room temperature at an initial strain rate of 1×10^{-3} s^{-1}. Two types of flat specimens for each homogenized alloy were cut by electron discharging machining along the rolling direction. The first type of tensile specimens with a total length of 60 mm (gauge length of 30 mm, gauge width of 5 mm) and a thickness of 2 mm were used to probe the bulk tensile properties. Another type of flat dog-bone shaped tensile specimens with a total length of 20 mm (gauge length of 10 mm, gauge width of 2 mm) and a thickness of 1 mm were used to measure the local strain evolution by digital image correlation (DIC) method with a Kammrath & Weiss tensile stage and an Aramis system (GOM GmbH, http://www.gom.com/metrology-systems/system-overview/aramis.html). At least five samples for each condition were tested to confirm reproducibility.

Magnetic behavior characterization: The temperature dependence of magnetization *M(T)H* of the present HEAs was measured by using a Physical Properties Measurement System (PPMS 9, Quantum Design) equipped with a standard vibrating sample magnetometry (VSM) option. The cuboid specimens for magnetic measurement were prepared in 3 × 3 × 1 mm^3 with all the surfaces grounded by silicon carbide paper to 2500#. The *M(T)H* dependence was measured under an applied magnetic field of 100 Oe in a temperature range from 300 K to 1000 K. The temperature-sweeping rate was 20 K/min. Hysteresis loops *M(H)T* were taken at 300 K, 573 K, 673 K, 773 K and 873 K in an external magnetic field of ± 10000 Oe. The magnetic field-

sweeping rate was 50 Oe/s. To achieve more accurate coercivity, the magnetic field-sweeping rate between the external magnetic field of ± 100 Oe was 2 Oe/s. At least three samples were tested for each condition.

The magnetic domain pattern was observed by magneto-optical Kerr effect (MOKE) microscopy (Zeiss Axio Imager.D2m evico magnetics GmbH) using longitudinal sensitivity. To analyze the domain wall motion, the electromagnet option of the MOKE microscope was used to apply magnetic field up to 1000 Oe. The image contrast was enhanced by subtracting the non-magnetic background image from the collected average image using KerrLab software.

Structural characterization: Multiple techniques were performed to analyze the detailed microstructure of the alloys. X-ray diffraction (XRD) measurements with Co K_{α} (wavelength=1.78897Å) were conducted using an X-ray diffractometer (D8 Advance 25-X1). The XRD data were analyzed using Bruker software (TOPAS Version 5.0) with a step size of $\Delta 2\theta$=0.009° and a count time of 224.64 s/step. Electron backscatter diffraction (EBSD) measurements were carried out on a Zeiss-Crossbeam XB 1540 focused ion beam scanning electron microscope (SEM) and analyzed with TSL OIM data-collection software (http://www.edax.com/Products/EBSD/OIM-Data-Collection-EBSD-SEM.aspx). Electron channeling contrast imaging (ECCI) was performed by a Zeiss-Merlin SEM. Conventional transmission electron microscopy (TEM) investigation including dark-field (DF)-TEM was conducted using JEOL JEM 2100+ TEM operated at 200 kV. The lattice strain distribution maps by 4D-STEM were collected by JEOL JEM 2200 TEM with a beam size of 1 nm. High-resolution (HR) TEM images were conducted using a C_s image-corrected FEI Titan Themis 60-300 operated at 300 kV. Atom probe tomography (APT) analysis was performed using a local electrode atom probe (LEAP 5000 XR) in laser-pulsing mode with a testing temperature of 60 K, a pulse repetition rate of 125 kHz, a pulse fraction of 20% and an evaporation detection rate of 0.6%. Image visualization and analysis software (IVAS 3.8.4, Cameca

Instruments Inc) was used for rebuilding the 3D reconstructions and data analysis. TEM and APT specimens were lifted out and prepared by a dual-beam focused ion beam technique (FEI Helios Nanolab 600i).

Evaluation of strengthening mechanisms: The yield strength values (σ_y) of the current HEAs were quantitatively evaluated by considering the contributions of different strengthening mechanisms based on the analytical model:

$$\sigma_y = \sigma_{base} + \sigma_{ss-Al} + \sigma_{precipitation} + \Delta\sigma_{gb}$$

where σ_{base} is the lattice friction stress of the base HEA (B-HEA) without Al addition, σ_{ss-Al} is the solid solution strengthening by Al dissolved in the alloy matrix, $\sigma_{precipitation}$ represents the precipitation strengthening, and $\Delta\sigma_{gb}$ refers to the grain boundary strengthening. The substitutional solid solution strengthening for the Al-containing HEAs caused by Al addition based on dislocation-solute elastic interactions can be evaluated by the formula:[1]

$$\Delta\sigma_{ss-Al} = \frac{MGc^{1/2}\left|\frac{\varepsilon_G}{1+1/2|\varepsilon_G|} - 3\varepsilon_a\right|^{3/2}}{700}$$

where *M* is the Taylor factor (3.06 for fcc polycrystalline), *G* is the shear modulus of the fcc phase (*G* = 84 GPa, adopted from the fcc FeCoNiCr HEA),[2] and *c* is the total molar ratio of Al. ε_G and ε_a quantify the effects of elastic modulus and atomic size mismatch are defined as $\varepsilon_G = \frac{1}{G}\frac{\partial G}{\partial c}$ and $\varepsilon_a = \frac{1}{a}\frac{\partial a}{\partial c}$, respectively, and *a* stands for the lattice constant of the fcc phase. The ε_G is usually negligible compared to ε_a.

Precipitate shearing mechanism is also critically important for the strengthening of the current Al-containing HEAs due to the coherency between the nanoprecipitates and the matrix. Generally, three effects, namely particle-matrix coherency, modulus mismatch and atomic ordering, are considered as the main contributing factors for the precipitate shearing-related strengthening. Both the particle-matrix coherency and the modulus mismatch contribute prior to shearing while the atomic ordering contributes to the shearing process.[3] Accordingly, the

contribution of the precipitation strengthening is determined by comparing the strength contribution prior to the shearing (particle-matrix coherency plus the modulus mismatch) and that during the shearing (atomic ordering), i.e., the larger one is considered as the final contribution. The various contributions can be evaluated based on the following equations:[4]

$$\Delta\sigma_{Particle-matrix\ coherency} = M \cdot \alpha_{\varepsilon}(G \cdot \varepsilon)^{3/2}(\frac{2rf}{Gb})^{1/2}$$

$$\Delta\sigma_{Modulus\ mismatch} = M \cdot 0.0055(\Delta G)^{\frac{3}{2}}\left(\frac{2f}{G}\right)^{\frac{1}{2}}\left(\frac{r}{b}\right)^{\frac{3m}{2}-1}$$

$$\Delta\sigma_{Atomic\ ordering} = 0.81M(\frac{\gamma_{APB}}{2b})(\frac{3\pi f}{8})^{1/2}$$

where $b = \sqrt{2}a/2$ is the magnitude of the Burgers vector of the matrix, γ_{APB} is the anti-phase boundary energy of the precipitates (γ_{APB}=0.20 J/m^2, adopted from $Ni_3(Al,Ti)$ in Ni-based superalloys,[5] which has a similar crystal structure as the $L1_2$ phase), f is the volume fraction of the precipitates, r is the average precipitate radius, ΔG is the shear modulus mismatch between matrix and precipitates (G =77 GPa is adopted from $Ni_3(Al,Ti)$).[6]

The contribution of grain boundary strengthening can be calculated by:[7, 8]

$$\sigma_{gb} = k_{\mathrm{HPS}}\, d^{-1/2}$$

where k_{HPS} represents the Hall-Petch slope (494 MPa · μm$^{1/2}$, adopted from the fcc FeCoNiCrMn HEA).[9] The average grain sizes in the HEA samples with both excluding and including annealing twin boundaries are listed in **Table S**2. Considering the facts that the difference in average grain sizes of excluding and including annealing twin boundaries for each composition is relatively small (<9%), and the Hall-Petch slope adopted from the reference [9] is for the case of excluding annealing twin boundaries, we thus calculated the grain boundary strengthening σ_{gb} using the grain size values excluding annealing twin boundaries in the present study.

References

[1] R. L. Fleischer, *Acta Metall.* **1963**, 11, 203.

[2] Z. Wu, H. Bei, G. M. Pharr, E. P. George, *Acta Mater.* **2014**, 81, 428.

[3] H. Wen, T. D. Topping, D. Isheim, D. N. Seidman, E. J. Lavernia, *Acta Mater.* **2013**, 61, 2769.

[4] A. J. Ardell, *Metall. Mater. Trans. A* **1985**, 16, 2131.

[5] R. Kozar, A. Suzuki, W. Milligan, J. Schirra, M. Savage, T. Pollock, *Metall. Mater. Trans. A* **2009**, 40, 1588.

[6] T. Pollock, A. Argon, *Acta Metall. Mater.* **1992**, 40, 1.

[7] E. Hall, *Proc. Phys. Soc., B* **1951**, 64, 747.

[8] N. Petch, *J. Iron Steel Inst., London* **1953**, 174, 25.

[9] F. Otto, A. Dlouhý, C. Somsen, H. Bei, G. Eggeler, E. P. George, *Acta Mater.* **2013**, 61, 5743.

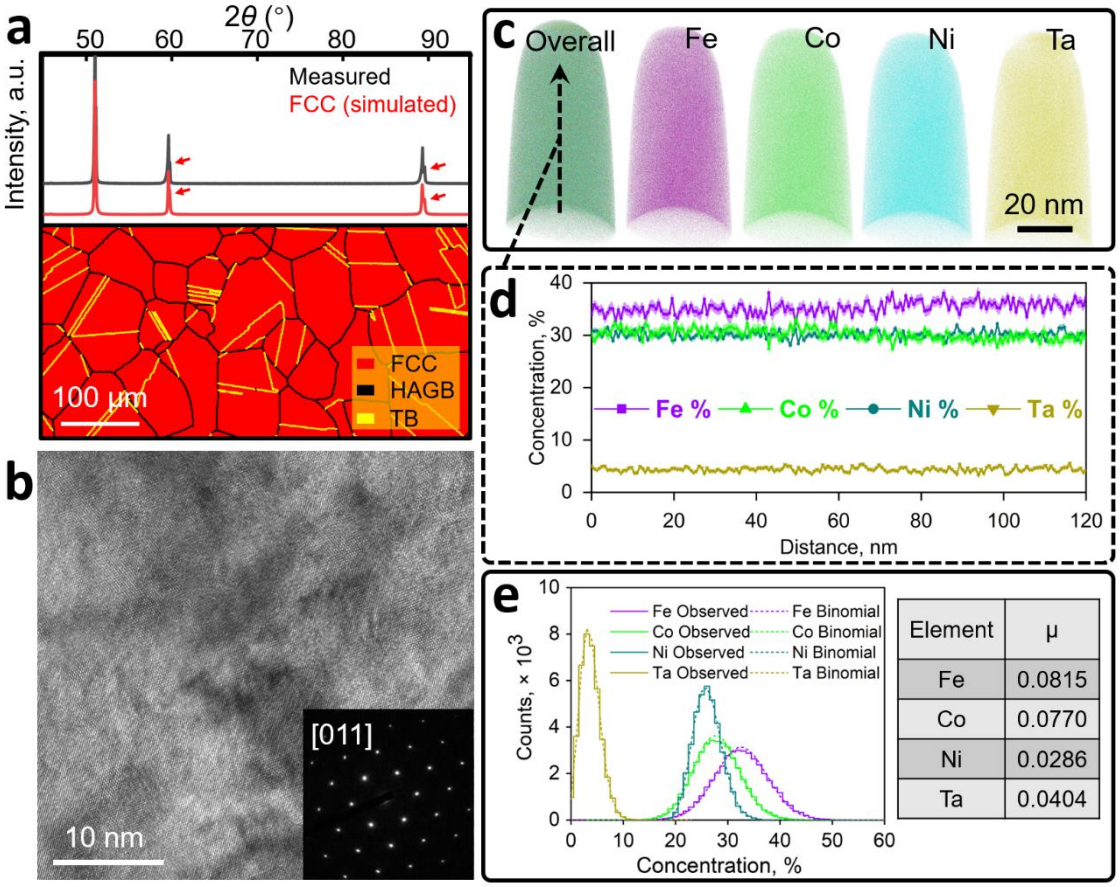

Figure S1. Microstructure of the B-HEA from micro- to near atomic-scale. a, XRD pattern and EBSD phase map. **b,** TEM image showing a precipitate-free microstructure. The inset SAED pattern confirms the fcc structure with the zone axis of [011]. **c,** 3D reconstruction maps of a typical APT tip showing the uniform distribution of all elements in near atomic-scale. **d,** 1D compositional profiles across the tip with the direction marked by the black arrow in (**c**). **e,** Frequency distribution analysis confirming the random distribution of the elements.

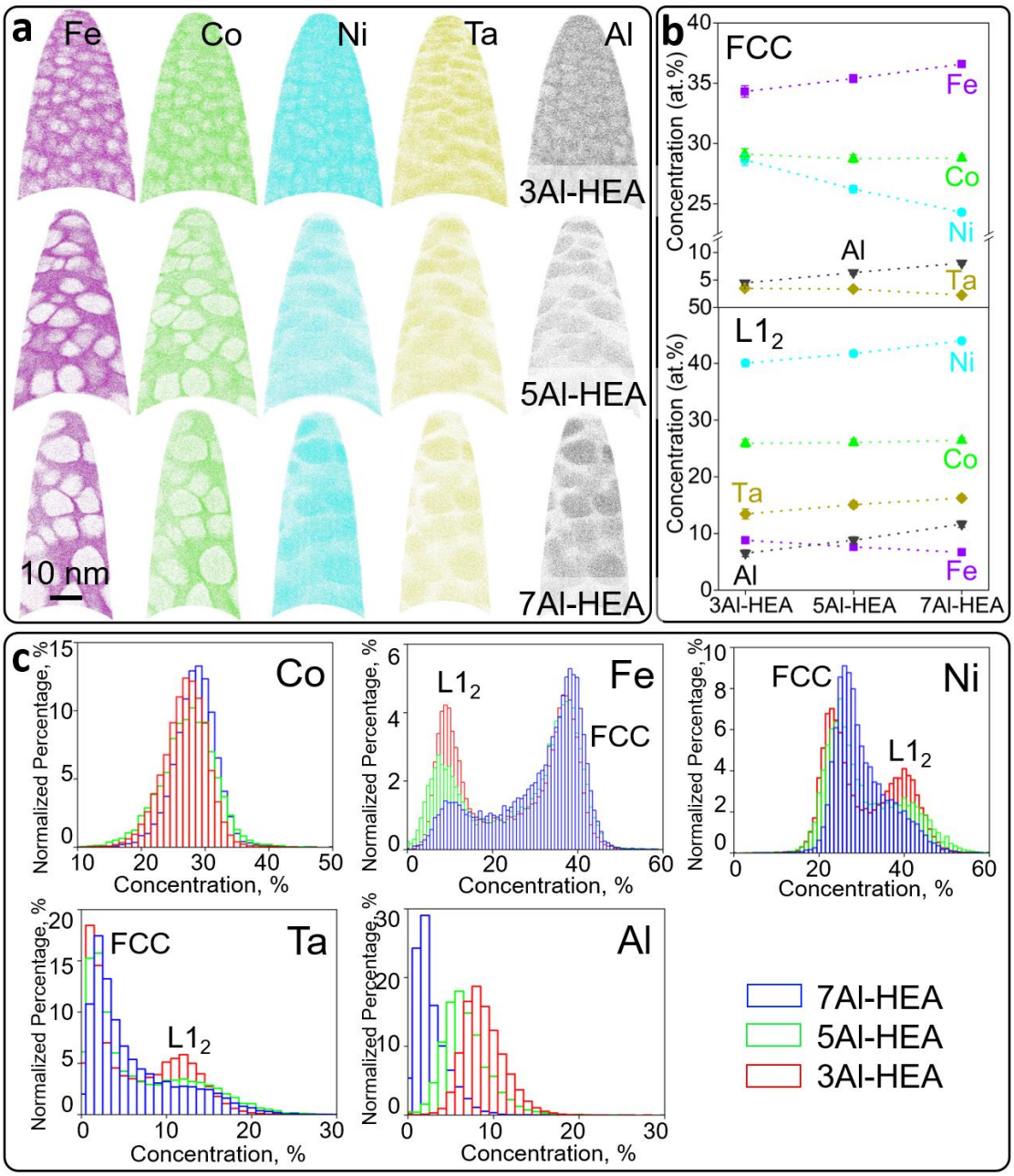

Figure S2. Structure and composition of the Al-containing HEAs. a, Thin slice from 3D reconstruction of the APT data sets, showing the variation in size and number density of the precipitates in different alloys. **b**, Average chemical compositions of the fcc and L12 phases acquired from the APT sub-volumes. **c**, Voxelization and threshold calculation of the atom distribution.

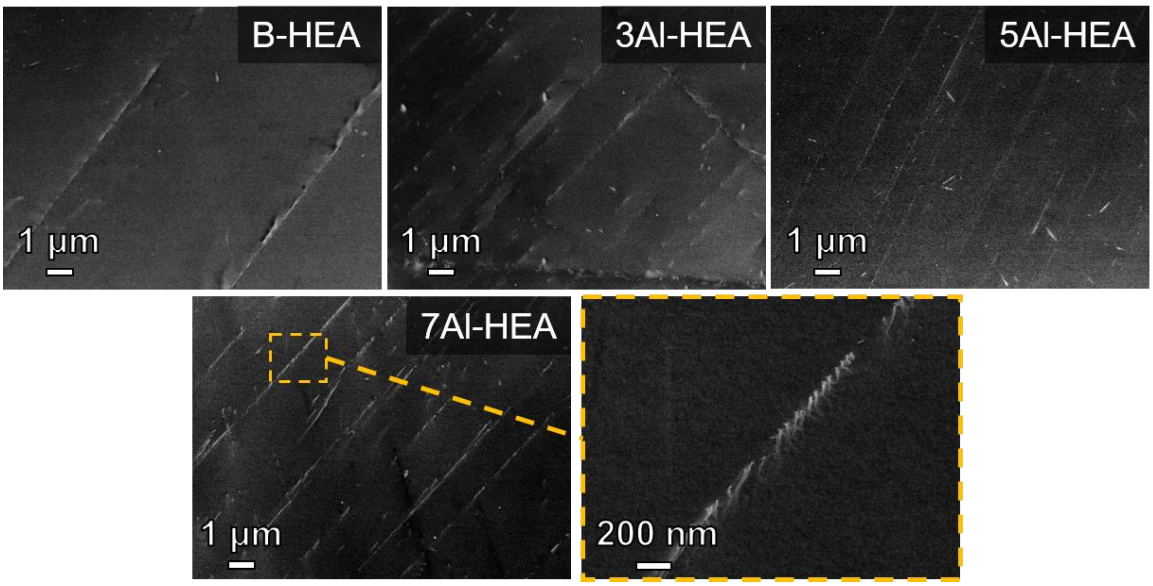

Figure S3. Typical ECC images of the B-HEA, 3Al-HEA, 5Al-HEA and 7Al-HEA at 5% local strain. The zoom-in image of the orange dashed square region shows a group of dislocations in a long pile-up configuration, coming from the same Frank-Read. The dislocation pattern shows a modest pairing configuration which might elude to local short-range order effects.

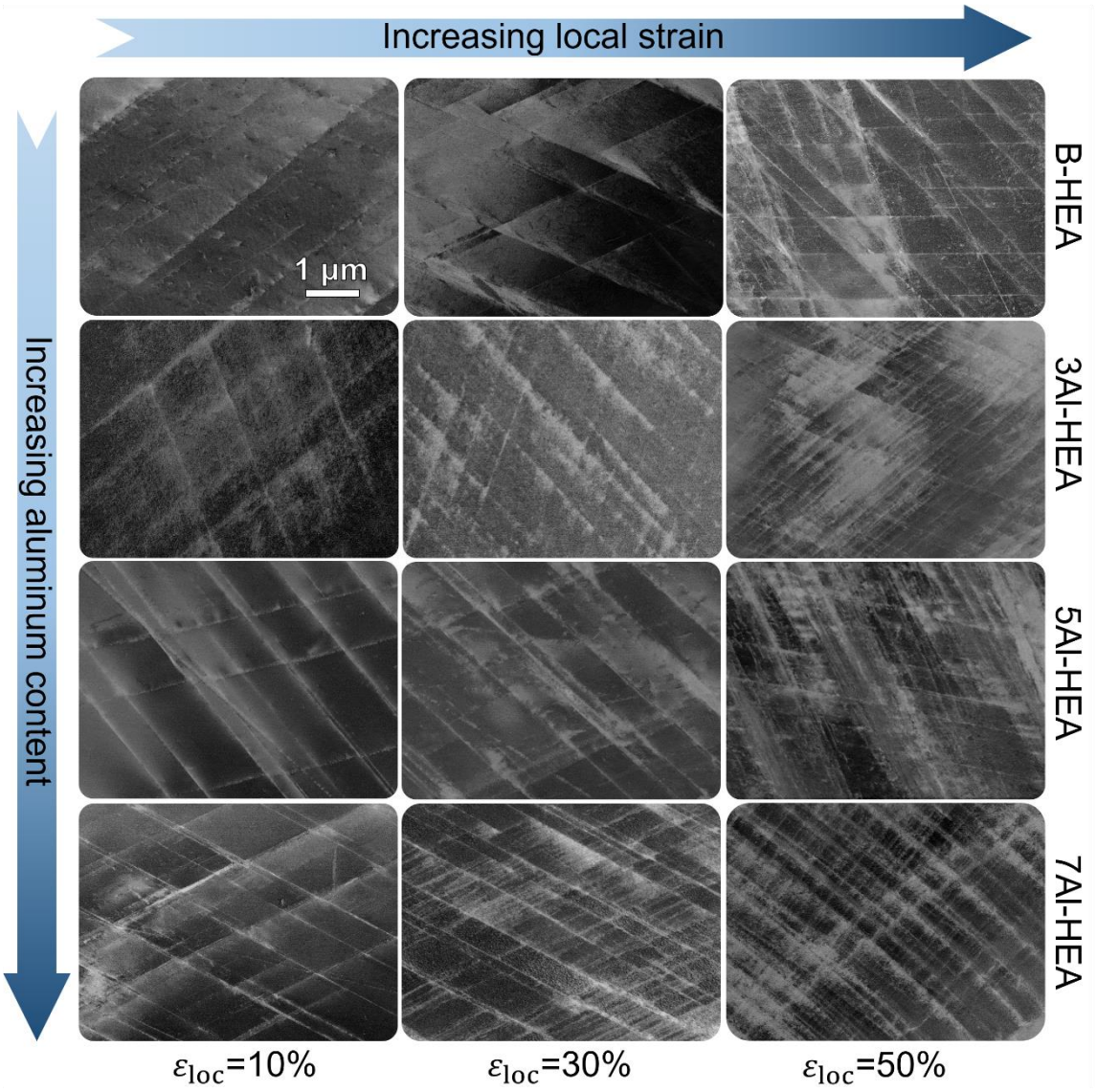

Figure S4. ECC images showing the deformation microstructures in the HEAs with various aluminum contents at different local strain (ε_{loc}) levels.

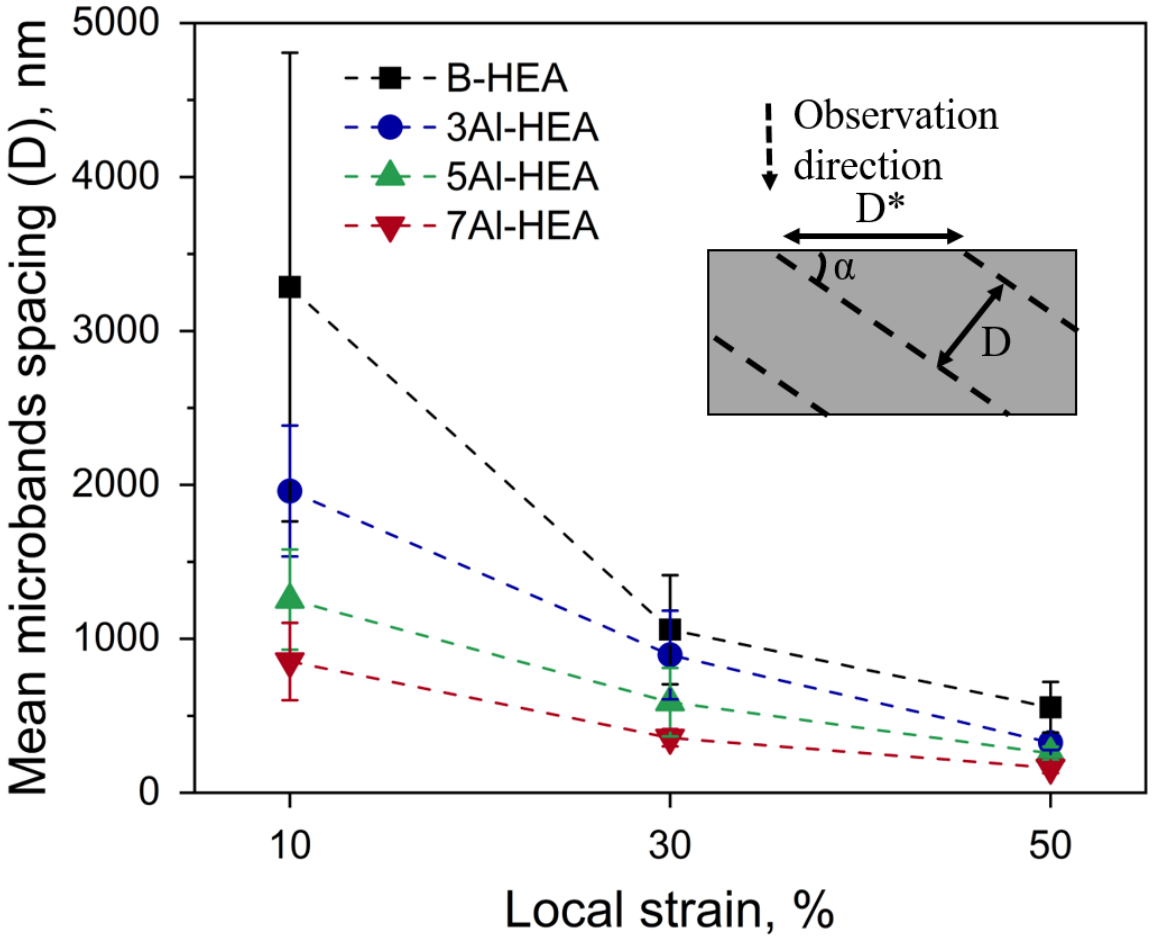

Figure S5. Quantification of the decreases in mean microband spacing with increasing local strain. The inset shows the correction of the microband spacing using the equation $D=\sin(\beta)\cdot D^*$, where D is the actual microband spacing, D* is the measured microband spacing under ECCI observation and β is the inclination angle of the microbands to the sample surface acquired by EBSD.

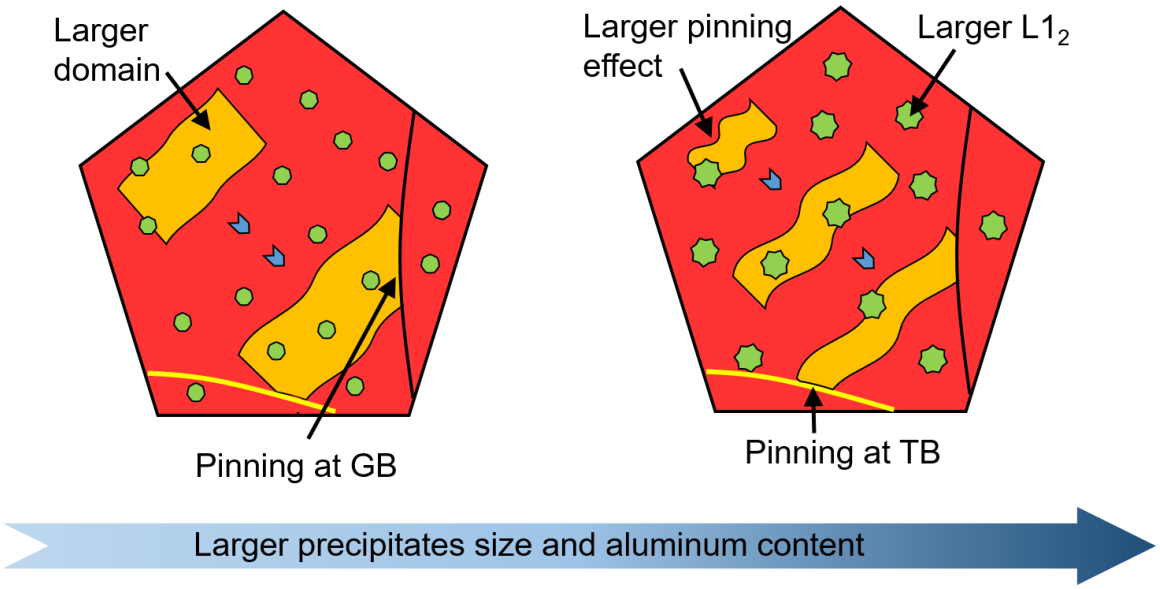

Figure S6. Schematic illustration of the domain walls' movement and pinning mechanisms in the HEAs with different precipitate sizes and aluminum contents. GB and TB stand for grain and twin boundaries, respectively.

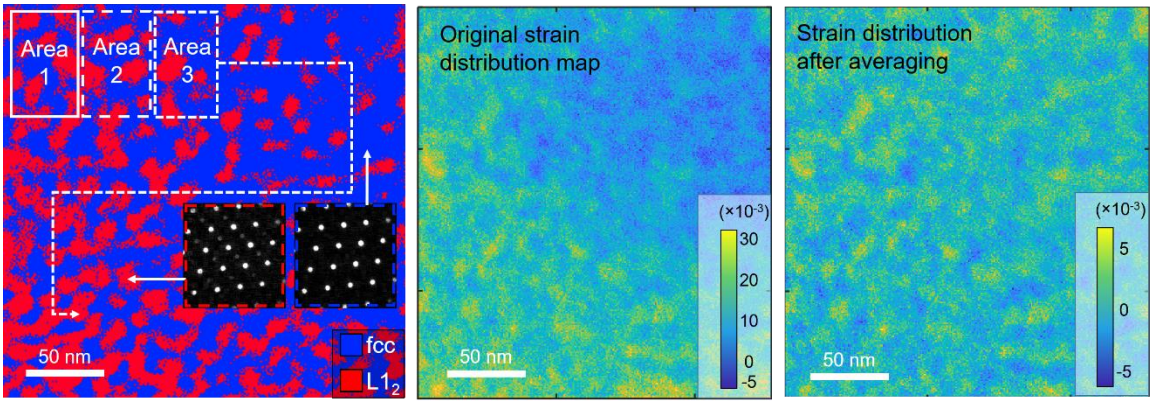

Figure S7. Illustration of the method for determining the lattice strain distribution among the $L1_2$ nanoprecipitates and the fcc matrix based on 4D-STEM measurements. The overall strain is calculated by subtracting and averaging the strain of each small area.

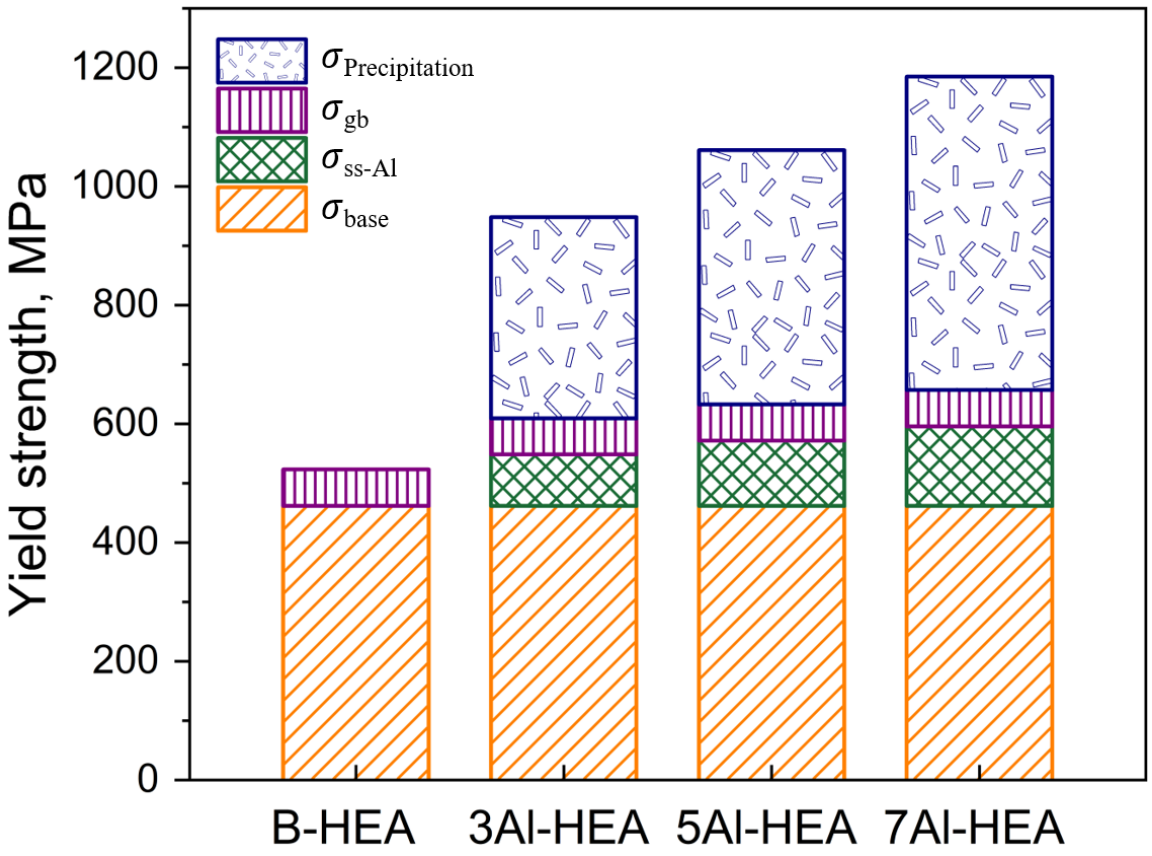

Figure S8. The theoretical calculation results on the contributions of various strengthening effects to the yield strengths of the current HEAs.

Table S1. Bulk chemical compositions of the as-cast HEAs in atomic percent measured by inductively coupled plasma mass spectrometry.

Element (at%)	Co	Fe	Ni	Ta	Al
$Co_{30.0}Fe_{35.0}Ni_{30.0}Ta_{5.0}$	30.32	34.51	30.23	4.94	0.003
$Co_{29.0}Fe_{34.0}Ni_{29.0}Ta_{5.0}Al_{3.0}$	29.29	33.85	29.31	4.79	2.77
$Co_{28.3}Fe_{33.4}Ni_{28.3}Ta_{5.0}Al_{5.0}$	28.55	33.41	28.35	4.77	4.92
$Co_{27.7}Fe_{32.6}Ni_{27.7}Ta_{5.0}Al_{7.0}$	27.99	31.97	28.10	4.71	7.23

Table S2. The statistical data for the microstructures in the HEAs with various Al contents.

Alloy	Grain size (excluding annealing twin boundaries), μm	Grain size (including annealing twin boundaries), μm	Average precipitate size by TEM, nm	Average volume size of the precipitates by APT, nm^3	Al dissolved in the fcc matrix, at%
B-HEA	64.8 ± 9.8	61.8 ± 16.6	/	/	/
3Al-HEA	66.9 ± 12.8	63.8 ± 10.8	6.2 ± 0.9	168 ± 27	4.5
5Al-HEA	65.2 ± 10.4	60.5 ± 16.2	9.2 ± 18	1029 ± 54	6.3
7Al-HEA	65.3 ± 10.3	61.3 ± 15.0	13.5 ± 2.5	2294 ± 125	8.1